

See discussions, stats, and author profiles for this publication at: <https://www.researchgate.net/publication/274069731>

Facile Fabrication Of RGO/N-GZ Mixed Oxide Nanocomposite For Efficient Hydrogen Production Under Visible Light

ARTICLE in THE JOURNAL OF PHYSICAL CHEMISTRY C · MARCH 2015

Impact Factor: 4.77 · DOI: 10.1021/acs.jpcc.5b00311

CITATION

1

READS

241

3 AUTHORS:



Deepak Kumar Padhi

Institute of Minerals and Materials Technology

5 PUBLICATIONS 81 CITATIONS

[SEE PROFILE](#)



Kulamani Parida

ITER, Siksha 'O' Anusandhan University

346 PUBLICATIONS 6,806 CITATIONS

[SEE PROFILE](#)



Saroj Singh

Institute of Minerals and Materials Technology

70 PUBLICATIONS 391 CITATIONS

[SEE PROFILE](#)

Facile Fabrication Of RGO/N-GZ Mixed Oxide Nanocomposite For Efficient Hydrogen Production Under Visible Light

Deepak kumar Padhi,^{†,‡} Kulamani Parida,^{*,†,§} and S. K. Singh^{†,‡}

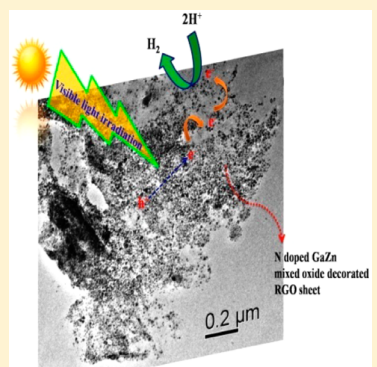
[†]Academy of Scientific and Innovative Research (AcSIR), Council of Scientific and Industrial Research, Anusandhan Bhawan, 2 Rafi Marg, New Delhi-110 001, India

[‡]Advanced Materials Technology Department, CSIR-Institute of Minerals and Materials Technology, Bhubaneswar-751 013, Odisha, India

[§]Centre for Nano Science and Nano Technology SOA University, Bhubaneswar-751 030, Odisha, India

Supporting Information

ABSTRACT: A series of reduced graphene oxide and N-doped GaZn mixed oxide nanocomposites (RGO/N-GZ) were fabricated by a facile chemical route. The adopted hydrothermal route results in reduction of graphene oxide (GO) to RGO as well as well decoration of nanostructure N-GZ mixed oxide on RGO sheets. 4 wt % loading of RGO to N-doped GZ mixed oxide showed highest amount of hydrogen production with an apparent quantum efficiency of 6.3% under visible light irradiation even if in absence of Co-catalyst. PL, TRPL, photocurrent measurement, and BET surface area analysis of N-GZ mixed oxide/RGO composite give the evidence for effective minimization of electron–hole recombination in comparison to neat N-GZ mixed oxides. The highest photocatalytic activity N-GZ/4RGO for hydrogen production is well explained on the basis of low PL intensity, longer average decay time (value of $\langle \tau \rangle$ for N-GZ and 4RGO/N-GZ is 3.74 and 5.76 ns, respectively), high photocurrent generation (50× more than N-GZ), large surface area and cocatalytic behavior of RGO.



1. INTRODUCTION

After the tremendous discovery of the photocatalytic property of TiO_2 by Fujisima and Honda in 1972, wide bandgap oxide semiconductors photocatalysis have been extensively studied for the conversion of solar energy to chemical energy.¹ In this regards, under visible light irradiation, hydrogen production from water using metal oxides, sulfides, oxynitrides, nanocomposites, and so on, photocatalysts is one the promising ways for the utilization of renewable source.^{2–8} Although oxide materials possesses good stability, nontoxicity, and cost-effective, but the wide band gap energy decreases their overall efficiency, which is the major drawback for commercial application.⁹ Hence, for the better utilization of solar spectrum, band gap engineering has been introduced for the tuning of band gap energy of metal oxide by many researchers.

Anion doping to metal oxide photocatalysts has created a lot of interest compared to cation doping, because cation doping possess thermal instability and create a platform for trapping of electron by the metal center which reduces its photocatalytic efficiency.^{10–13} In this contrast, among several anions doped material, nitrogen containing material have been extensively studied for photocatalytic application such as $GaN:ZnO$, $\beta\text{-Ge}_3\text{N}_4$, $Ta_3\text{N}_5$, $TaON$, and so on.^{14–17}

Although N doping to semiconductor material showed promising activity, their practical application is still limited due to their exhibition of low stability toward photocorrosion.^{18,19} Loading of noble metal can successfully minimize the electron–

hole recombination, but its high cost and toxicity limits the practical application.²⁰

Among the reported efficient nitrogen containing photocatalytic material, generally these contain either transition metal cations with a d^0 electronic configuration or typical metal cations with a d^{10} electronic configuration as a principal cation component.^{21–24} Arai et al. has reported that d^{10} metal oxides give a better platform for the generation of photogenerated electron at its sp conduction band with high mobility and shows outstanding photocatalytic activity.²⁵ The authors' group have already reported visible light responsive N-doped d^{10} based material like N-doped GaZn mixed oxide and N-doped $In_2\text{Ga}_3\text{ZnO}_7$ showing promising activity for hydrogen production under visible light irradiation.^{26–29}

In the recent years, the use of carbon scaffolds to increase the activity has created a lot of interest in the field of fuel technologies.³⁰ Among different carbon based materials, graphene has attracted a lot attention for its outstanding unique property like high surface area ($2600\text{ m}^2/\text{g}$), extreme thermal conductivity ($\sim 3000\text{--}5000\text{ W m}^{-1}\text{ k}^{-1}$), and excellent carrier mobility ($\sim 10000\text{ cm}^2\text{ V}^{-1}\text{ s}^{-1}$) at room temperature, good optical transparency ($\sim 97.7\%$), and high Young's modulus ($\sim 1\text{ TPa}$).^{31,32} By introducing graphene to metals, metal oxide, many researchers have explained that graphene

Received: January 12, 2015

Revised: February 27, 2015

Published: March 2, 2015

presence enhances photocatalytic efficiency of metal oxide like ZnO/RGO, TiO₂/RGO, Fe₃O₄/RGO, TiO₂/MoS₂-graphene, TiO₂ nanotube/RGO, Cu₂O/RGO, and so on.^{33–38} In this regard, the authors' group have also reported α -Fe₂O₃ nanorod/RGO, α -FeOOH nanorod/RGO, Gd(OH)₃ nanorod/RGO, and RGO/InGaZn nanocomposite for photocatalytic application.^{39–42}

In the case of graphene-based metal oxide hybrid material, the blackbody property of graphene increases the light harvesting capacity, which leads to better utilization of light energy for photochemical reaction. In addition to that, the extended π -electron conjugation of the carbon network of graphene sinks the photogenerated electron from the conduction band of metal oxide and channelizes through its framework. Thus, minimizes the electron–hole recombination and enhances the photocatalytic activity of metal oxide. To date hardly any N containing metal oxide/graphene nanocomposites have been reported for photocatalytic hydrogen production under visible light irradiation. It is expected that the interaction of graphene with N containing metal oxide will be more preferred for photocatalytic application compared to its interaction with the counterpart of metal oxides. To the best of our knowledge, the hybrid structure between graphene and N-GZ mixed oxide has not been reported so far.

Owing to the superior property of graphene and N containing d¹⁰ group of metal oxides, herein we have developed RGO/N-GaZn mixed oxide nanocomposite by a facile chemical route. All the synthesized RGO/N-GZ mixed oxide nanocomposites showed outstanding photocatalytic activity toward hydrogen production under visible light irradiation compared to our previous study on N-doped GaZn mixed oxide.²⁸ The various spectroscopic techniques have been carried out to evaluate the superior property of all the synthesized photocatalyst and discussed in detail.

2. EXPERIMENTAL SECTION

2.1. Materials. Gallium nitrate ($\text{Ga}(\text{NO}_3)_3$), zinc nitrate ($\text{Zn}(\text{NO}_3)_2$), glycine, natural graphite powder, and potassium permanganate (KMnO_4) were obtained from Sigma-Aldrich chemicals. Sulfuric acid (H_2SO_4), hydrochloric acid (HCl), sodium nitrate (NaNO_3), hydrogen peroxide (H_2O_2), and sodium hydroxide (NaOH) were procured from Finar Chemicals Limited. All these above chemicals were used as such without further purification.

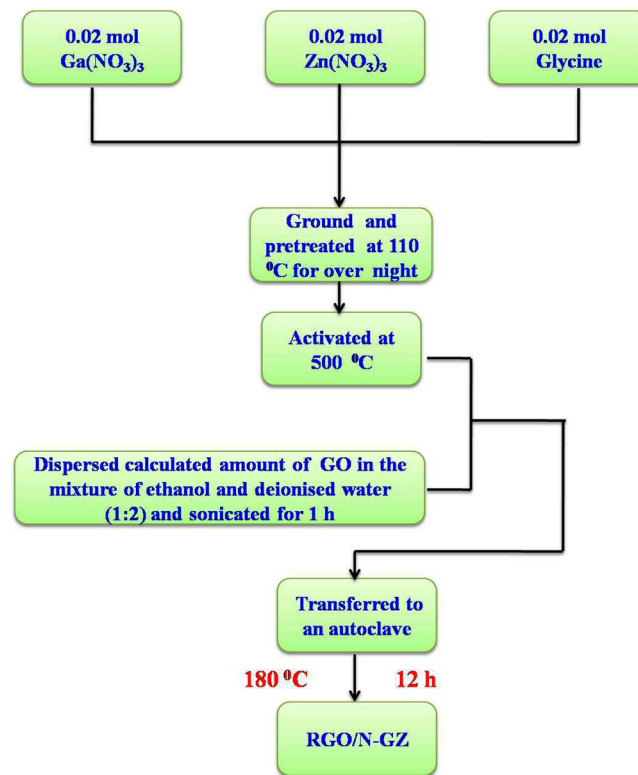
2.2. Synthesis of Graphene Oxide (GO). Graphene oxide was prepared by reported modified Hummers method.⁴³ Briefly, 2 g of graphite powder with 1 g of NaNO₃ was suspended in 92 mL of concentrated H₂SO₄, stirred for 30 min, and its container was put in an ice bath. To start the oxidation process, 32 g of KMnO₄ was added slowly to obtain a purple-green color solution, which indicates the completion of the oxidation process. Then, the temperature of the suspension was maintained around 40 °C by transferring the container into a water bath and stirring for 90 min. About 200 mL of deionized water was added to the solution and stirred for 30 min. A total of 30 mL of 30% H₂O₂ solution was slowly added to it and a golden-brown sol was obtained. Then, 200 mL of deionized water was added to the golden-brown sol and it was centrifuged. The resultant solution was washed with deionized water several times until the pH of the solution reached 6. Finally, the obtained sample was dried at 80 °C for 24 h.

2.3. Solid State Synthesis of N-Doped GZ Mixed Oxide. Nitrogen-doped GaZn mixed oxides were prepared by

solid state reaction method reported by our group.²⁸ Briefly, a calculated amount of $\text{Ga}(\text{NO}_3)_3$, $\text{Zn}(\text{NO}_3)_2$, and glycine were mixed in the molar ratio 2:1:2. The mixture was ground and pretreated at 110 °C for overnight. Then the obtained mixture was activated at 500 °C for 5 h where as neat GaZn mixed oxide was prepared by the same method without using glycine. The obtained sample was designed as GZ.

2.4. Hydrothermal Synthesis of RGO/N-GZ Mixed Oxide. In a typical experiment, calculated amount of GO was dispersed in 45 mL mixture of ethanol and deionized water [where the volume ratio of ethanol and deionized water = 1:2] for 1 h. Then, the prepared N-doped GaZn mixed oxide was added to the obtained brown color of GO suspension and stirred for 30 min. The suspensions were transferred to Teflon autoclave, followed by hydrothermal treatment at 180 °C for 12 h. The obtained product was centrifuged, washed with deionized water and dried at 80 °C for 24 h. The above process is illustrated in Scheme 1. The obtained sample is

Scheme 1. Schematic Representation of the Fabrication of RGO/N-GZ Nanocomposite



designated as RGO/N-GZ. The as synthesized RGO/N-GZ nanocomposites with various amount of GO, that is, 1, 3, 4, and 5 wt % to N-GaZn mixed oxide are designated as 1RGO/N-GZ, 3RGO/N-N-GZ, 4RGO/N-GZ, and 5RGO/N-GZ, respectively.

2.5. Photocatalytic Water Splitting Procedure. An inner irradiation type reactor was used to carry out the photocatalytic reaction. For photocatalytic water splitting experiment, 0.05 g of powder photocatalysts was suspended in 50 mL of an aqueous solution containing 10 vol % of CH₃OH solution. The solution was kept under stirring with a magnetic stirrer to inhibit particles to settle at the bottom of the reactor. Before irradiation of light to the reactor, first the reactant solution was first evacuated several times to ensure

complete removal of air by purging with nitrogen gas. The Hg visible lamp of 125 W medium pressures was used as irradiation source and also 1 mol L⁻¹ NaNO₂ solution was introduced into the water jacket as an internal circulation cooling medium to eliminate light with a wavelength shorter than 400 nm. The evolved gas was collected by water displacement technique and analyzed by GC-17A using 5 Å molecular sieve column with a thermal conductivity detector (TCD).

3. ANALYTICAL CHARACTERIZATION

All the synthesized photocatalysts were characterized by PXRD, FTIR, Raman, DRUV-vis, TEM, PL, XPS, BET surface area, and photoelectrochemical measurement techniques. Rigaku Miniflex (set at 30 kV and 15 mA) was used to record the powder X-ray diffraction (PXRD) over the range $10^\circ < 2\theta < 60^\circ$ with a scan rate of $2^\circ/\text{min}$ using Cu K α radiation ($\lambda = 1.54 \text{ \AA}$). The optical absorbance of all the samples was measured in the region 400–800 nm using UV-vis spectrophotometer (Varian Cary 100) with boric acid as the reference. X-ray photoelectron spectroscopy (XPS) analysis was carried out using VG Microtech Multilab ESCA 3000 spectrometer with a nonmonochromatized Mg K α X-ray source and C 1s peak of carbon at 284.9 eV was taken as reference for correction of the binding energy. Fourier transform infrared (FT-IR) spectrum of all the samples was recorded on Bruker ALPHA FT-IR spectrometer by taking KBr as the reference sample. Transmission electron microscopy (TEM) and high resolution transmission electron microscopy (HRTEM) images were taken on Philips TECNAI G² instrument at an accelerating voltage of 200 kV. For TEM analysis, the powder particles were dispersed with ethanol solvent and a very little amount was dripped on the copper grid and then it was coated with carbon film of 3 mm diameter fine-mesh. LS 55 fluorescence spectrometer (Perkin Elmer) was used to record the photoluminescence spectra of all the samples at room temperature with excitation at 350 nm. The photoelectrochemical measurement of all the samples was done using a potentiostat/galvanostat (Versastat 3, Princeton Applied Research). Briefly, a pyrex electrochemical cell is consisted of Ag/AgCl electrode and a platinum wire as reference and counter electrode, respectively. In this cell, the prepared electrode as working electrode and its potential was controlled by a potentiostat. An aqueous solution of Na₂SO₄ (0.1 M) at pH = 6 was taken in the cell and current voltage was measured under illumination conditions ($\lambda \geq 400 \text{ nm}$) by potentiostat/galvanostat (Versastat 3, Princeton Applied Research). No photoresponse in the solution was observed by FTO.

4. RESULTS AND DISCUSSIONS

4.1. Structural Characterization. Figure 1 illustrates the XRD pattern of the synthesized samples. The crystallinity and phase pure characteristics of N-doped GZ mixed oxide is well matched with the spinel of Zn and Ga, that is, JCPDS file No. 86-0415. The obtained XRD result is also well matched with Ikarashi et al.⁴⁴ and also our previous report.²⁸ There is no change in its crystallinity and phase purity loading up to 5 wt % of RGO. But, RGO characteristics peak is not observed due to the highly intense diffraction pattern of N-GZ mixed oxide as well as the presence in very low amount.³⁹ The observed strongest peak at $2\theta = 22$ of GZ, that is, (311) becomes more intense N doping. The successful replacement O with N did

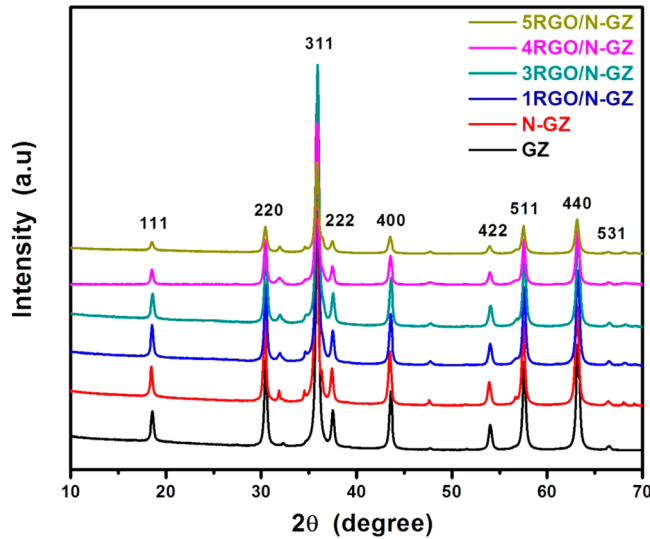


Figure 1. XRD patterns of all synthesized GZ, N-GZ, and RGO/N-GZ mixed oxide nanocomposites.

not cause any rebuilding block in the crystal lattice of GZ mixed oxide.

4.2. TEM Analysis. To know the morphological characteristics of the photocatalysts, TEM analysis has been carried out. Figure 2a–c displays the TEM images of N-GZ and 4RGO/N-GZ composite. An aggregated and irregular nanoparticles with average size $20 \pm 0.9 \text{ nm}$ of N-doped GZ mixed oxide was observed. The TEM images of 4RGO/N-GZ shows the well dispersion of N-GZ mixed oxide nanoparticles over reduced graphene oxide surface and its average particle size was observed to be $16 \pm 1 \text{ nm}$. The oxygenated functional moieties of GO facilitate for the homogeneous anchoring of N-GZ mixed oxide nanoparticles on its flat 2D surface which leads to decrease the restacking of graphene sheets and increase the stability of individual graphene sheets.⁴⁵ This stability of RGO with well anchored mixed oxide nanoparticles played a vital role in the enhanced photocatalytic activity of RGO/N-GZ composite. In case of 4RGO/N-GZ composite, the hydrothermal synthesis process hardly affects the morphology of N-GZ nanoparticles. A good interfacial contact of N-GZ nanoparticles on graphene sheets is also obtained during hydrothermal synthesis process. This strong interaction favors the facile transfer of the photoexcited electrons from the conduction band of N-GZ nanoparticles to the graphene sheets, which leads to minimizing the electron–hole recombination and hence enhances the photocatalytic activity. Figure 2c represents the selected area electron diffraction (SAED) pattern of 4RGO/N-GZ. Several bright continuous concentric rings can be clearly seen and those are the results of diffraction from the (220), (400), (511), and (440) planes of N-GZ mixed oxide, which is consistent with the XRD data. Thus, the polycrystalline nature of 4RGO/N-GZ photocatalyst is confirmed from its SAED pattern. Briefly, TEM analysis summarizes the following points: (1) Well-anchored N-GZ mixed oxide nanoparticles on graphene sheets are obtained by hydrothermal synthesis process; (2) The well decorated and good interfacial contact of N-GZ mixed oxide nanoparticles and graphene sheets leads to avoid the restacking of graphene sheets and, hence, increases the stability of individual graphene sheets; (3) Flat 2D-surface of graphene can easily sink the photoexcited electrons from the conduction band and

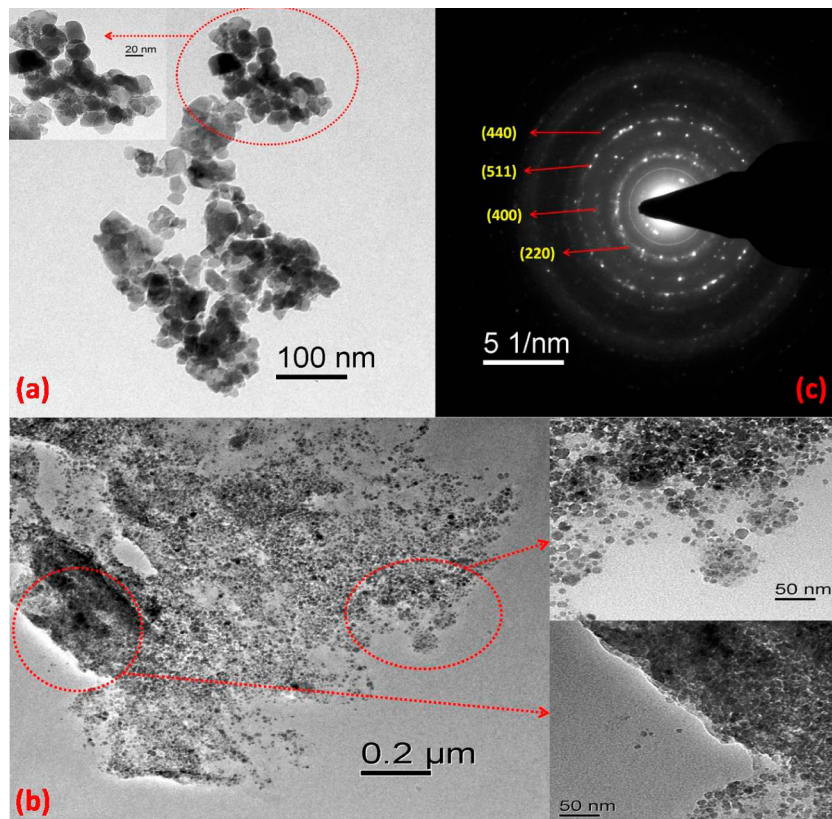


Figure 2. TEM images of (a) N-GZ mixed oxide, (b) RGO/N-GZ mixed oxide nanocomposite, and (c) SAED pattern of RGO/N-GZ mixed oxide.

channelizes it through π -conjugated network for the minimization of electron–hole recombination and enhances the photocatalytic activity of N-GZ mixed oxide nanoparticles.

4.3. DRUV-vis Spectra. DRUV-vis spectra analysis has been carried out to know the optical absorption property of all the photocatalysts. Figure 3a displays the optical absorbance spectra of all the photocatalysts. From the spectra, it has been observed that GZ mixed oxide could able to absorb UV light. The absorption of neat GZ mixed oxide was observed at 298 nm. But the adsorption edge of N-doped GZ oxide was observed at higher wavelength compared to the neat GZ mixed oxide i.e. 477 nm. The red shifting of absorption edge is attributed to nitrogen doping to the GZ mixed oxide which is very similar to our previous observation.²⁸ All the graphene loaded N-doped GZ mixed oxide photocatalysts showed slight larger absorption edge which is due to the blackbody property of RGO sheets.⁴⁶ This also suggests about the reduction of the oxygenated functional moieties (Hydroxyl, Carboxyl and Epoxy group) of GO by hydrothermal treatment and simultaneous conversion of GO to RGO during composite formation.³⁹ In addition to that, this evidence further suggests that during photochemical process the presence of RGO increases the surface electric charge of N-doped GZ mixed oxide which leads to indirect modification of its fundamental process of electro-hole pair formation.⁴⁶

The band gap energy of GZ, N-doped GZ mixed oxide, and all N-doped GZ-RGO composite is calculated by using the following equation.⁴²

$$ah\nu = A(h\nu - E_g)^n$$

where a , n , A , and E_g are the absorption coefficient, light frequency, proportionality constant, and band gap energy,

respectively. Herein, n describes the type of transition in a semiconductor, that is, $n = 1/2$ for direct transition and $n = 2$ for indirect transition. By using the method described earlier, the value of n for all the prepared mixed oxide photocatalysts, was determined to be $1/2$. It suggests the optical transition of RGO/N-GZ nanocomposites is directly allowed.⁴² From the plot of $(ah\nu)^n$ versus $h\nu$, the band gap is estimated by extrapolating the straight line to the X axis intercept and is shown in Figure 3b. The band gap energy of GZ was found to be 4.1 eV, whereas after N doping, GZ mixed oxide shows 2.6 eV. This reduction in the band gap energy is achieved due to the successful doping of N to GZ mixed oxide, which is quite similar to our previous report.²⁸ In addition to this, a very minimal variation in their band gap energy is observed up to 5 wt % loading of RGO to N-GZ mixed oxide (Figure 3b).

This band gap energy estimation confirms that the optical absorption properties of N-GZ mixed oxides are not strongly affected upon the complexation with RGO. But, RGO presence tends to shift the absorption band edge of N-GZ mixed oxides toward the red region.⁴⁷

4.4. XPS Spectra. The XPS spectra of 4RGO/N-GZ mixed oxide have been recorded to investigate the chemical composition and oxidation state of each element in the synthesized sample. Figure 4 represents the core level XPS spectra of N 1s, C 1s, O 1s, Ga 3d and Zn 2p in 4RGO/N-GZ nanocomposite. The N 1s peak is observed at 397.5 eV which can be attributed to substitution of N in N-GZ mixed oxide which is well in agreement with N-doped titania, reported by Valentin et al.⁴⁸ The C 1s peak observed at 284.7 eV was deconvoluted into two main peaks at binding energy values of 284.7 and 287.1 eV to give the strong evidence of the reduction of GO to RGO. The peak at the binding energy value of 284.7

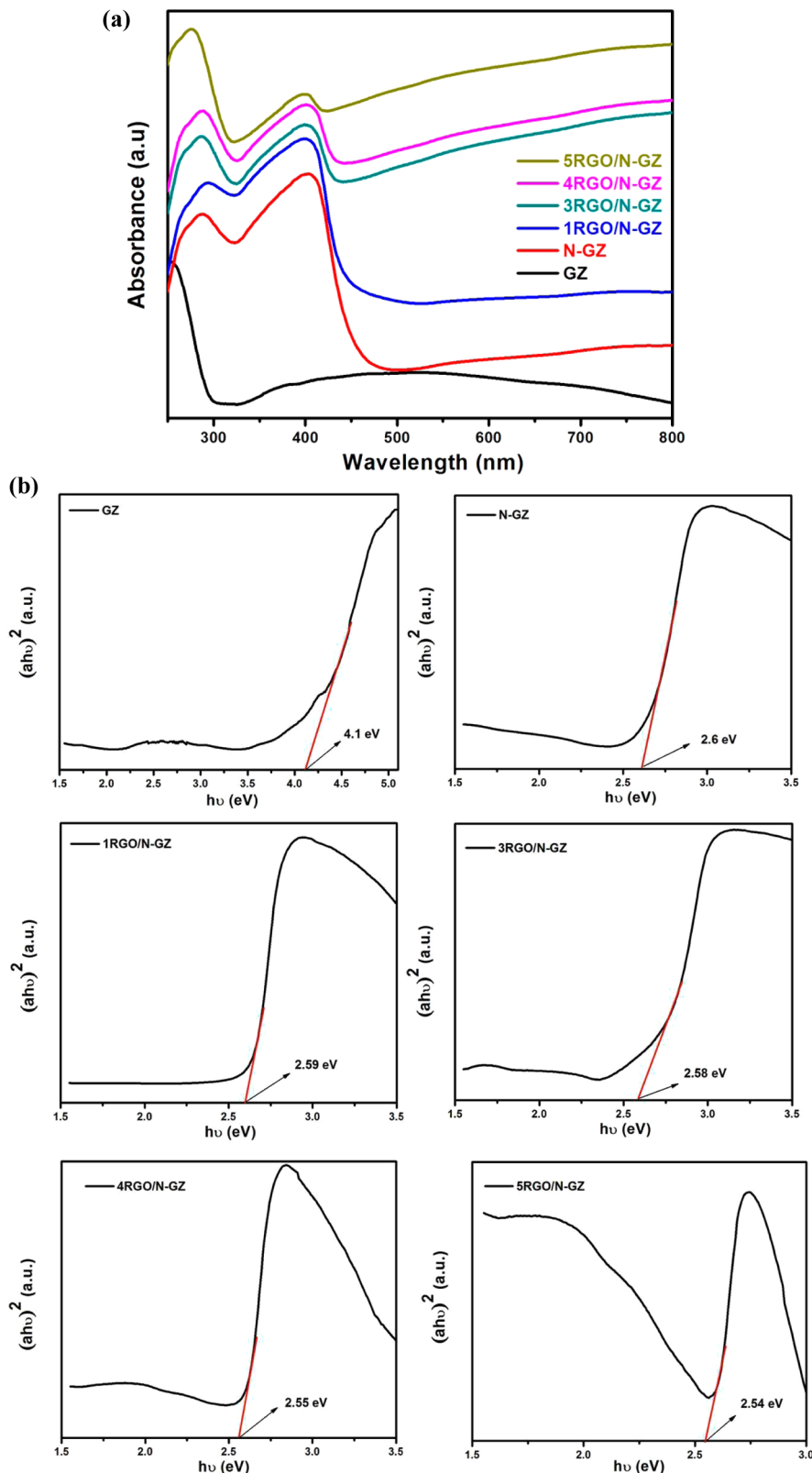


Figure 3. (a) Diffuse reflectance spectra of synthesized GZ, N-GZ mixed oxide, and RGO-loaded N-GZ mixed oxide. (b) Estimated band gap energy of synthesized GZ, N-GZ, and RGO-loaded N-GZ mixed oxide.

eV is assigned to sp^2 carbon of RGO and 287.1 eV is assigned to the oxygenated carbon species of reduced graphene oxide, such as $\text{C}-\text{OH}$ and $\text{C}=\text{O}$, respectively.^{49,50} The observed intensity C 1s spectra is much weaker in comparison to our

reported C 1s in GO.⁵¹ These results clearly suggest that the oxygenated functionalities of GO are significantly reduced in the case of 4RGO/N-GZ.^{51,52} Further, to give the evidence for the presence of lattice oxygen, we have deconvoluted the O 1s

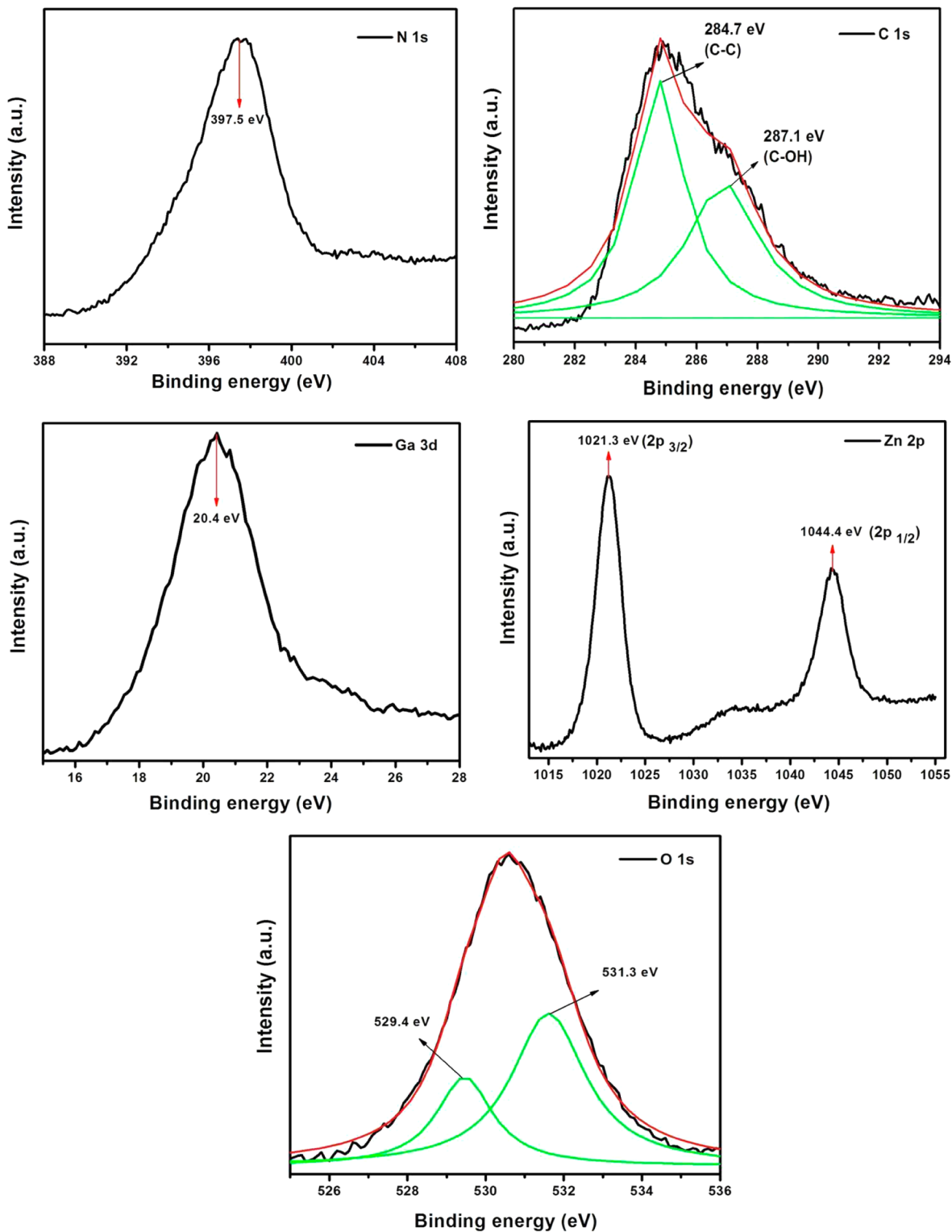


Figure 4. N 1s, C 1s, Ga 3d, In 3d, Zn 2p, and O 1s XPS spectra of 4RGO/N-GZ nanocomposite.

peak in to two individual peaks and the peak observed at 529.4 eV is attributed to the lattice oxygen.⁴²

The individual XPS scan for Ga 3d shows a peak at 20.4 eV that shows the presence of Ga in +3 oxidation state in 4RGO/N-GZ.²⁸ But for In 3d, two individual peaks positioned at 444.6 and 452.1 eV was observed and are assigned to In $3d_{5/2}$ and In $3d_{3/2}$ which confirms the presence of In in +3 oxidation state.⁴² The high resolution XPS scan for Zn 2p shows two individual

symmetric peaks positioned at 1021.4 and 1044.5 eV are assigned to Zn $2p_{3/2}$ and Zn $2p_{1/2}$, respectively, which confirms the presence of Zn in +2 oxidation state as the peak separation between the Zn $2p_{3/2}$ and Zn $2p_{1/2}$ is 23.1 eV.²⁸

4.5. Raman Analysis. In order to confirm the reduction GO to RGO as well as 4RGO/N-GZ composite formation, Raman analysis has been carried out (Figure 5). In the Raman spectra of GO, the peak observed at 1353 and 1590 cm^{-1} can

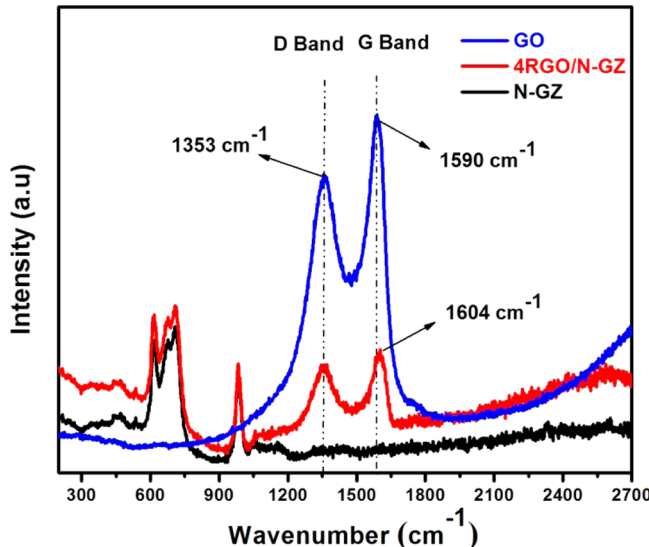


Figure 5. Raman spectra of synthesized GO, N-GZ mixed oxide, and 4RGO/N-GZ mixed oxide nanocomposite.

be assigned to its “D” and “G” band, respectively.⁵³ The D band suggests defects and disordering atomic arrangements of sp^3 hybridized carbon atoms; the G band indicates the in-plane symmetric stretching motion of symmetric sp^2 hybridized carbon atoms of the 2D layer of GO.⁵⁴ Neat N-doped GZ mixed oxide shows Raman characteristic peaks at 462, 538, 615, 677, 711, and 981 cm^{-1} (Figure 5). The obtained peaks in the region of 300–1000 cm^{-1} are due the fundamental Raman vibration of N-doped GZ mixed oxide.^{55–57} For 4RGO/N-GZ, both the D and G bands of GO as well as all the fundamental Raman vibrations of N-GZ mixed oxide were observed, which confirms the composite formation during the hydrothermal process. In contrast, the shifting of the G band of GO and the increase in the value of the D and G band ratio (I_D/I_G) of 4RGO/N-GZ as compared with GO (Table 1) give strong

Table 1. Intensity Ratio of “D” and “G” Band (I_D/I_G) and Variation in the G Band Position of GO and 4RGO/N-GZ Mixed Oxide Composite

sample name	position of “G” band (cm^{-1})	I_D/I_G
GO	1590	0.827
4RGO/N-GZ	1604	0.912

evidence about the well incorporation of N-GZ mixed oxide between the monolayer of GO and confirms the reduction of GO to RGO.⁵⁸ The higher I_D/I_G value of 4RGO/N-GZ mixed oxide compared to GO further indicates the decrease of sp^2 domain of 2D-monolayer of GO.⁵² These above observations are consistent with our TEM and XPS analysis.

4.6. BET Surface Area Analysis. The BET surface area of neat N-GZ was found to be $48.3 \text{ m}^2/\text{g}$. But after introduction RGO to N-GZ, the surface area was found to be remarkably increased. All RGO/N-GZ nanocomposite photocatalysts showed higher surface area compared to neat N-GZ. Among all RGO/GZ photocatalysts, 4RGO/N-GZ exhibits the highest surface area of $96 \text{ m}^2/\text{g}$, whereas 1RGO/N-GZ, 3RGO/N-GZ, and 5RGO/N-GZ showed surface areas of 62, 73, and $58 \text{ m}^2/\text{g}$, respectively. The crystal growth inhibition effect of N-GZ nanoparticles in presence RGO is the possible reason for this increase in BET surface area of all nanocomposite.⁴² This BET

surface area results can be correlated with TEM study as the particle size and surface area are inversely related to each other. In our case, TEM results showed a N-GZ nanoparticles average particle size of $20 \pm 0.9 \text{ nm}$, whereas after introduction of 4 wt % RGO to N-GZ the average particle size of N-GZ nanoparticle is observed to be $16 \pm 1 \text{ nm}$, which is in good agreement with the surface area study. Hence, BET surface area analysis concludes that 4RGO/N-GZ nanocomposite showed high surface area which possesses more number of active sites on the surface for better adsorption of reactant molecules and ultimately enhances its photocatalytic activity.⁴² Further, for better convince the N_2 adsorption–desorption isotherm of all the prepared materials is shown in the Supporting Information (Figure S1). The obtained isotherm pattern showed type-IV and displays the mesoporous structures of all the synthesized photocatalysts due to the looplike nature of the nitrogen adsorption isotherm.

4.7. Photoluminescence Spectra. The photoluminescence spectra (PL) were measured to reveal the migration, transfer, and recombination processes of the photoinduced charge carriers (Figure 6). It is well known that PL intensity is

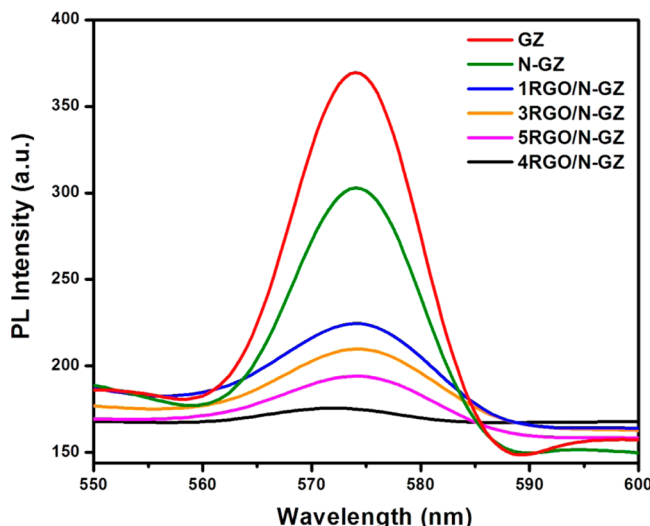


Figure 6. Photoluminescence spectra of GZ, N-GZ mixed oxide, and all RGO-loaded N-GZ mixed oxide nanocomposites.

directly interlinked to the rate of electron–hole recombination. The higher the PL intensity, the higher the rate of electron–hole recombination and vice versa.⁴² The PL intensity of neat GZ mixed oxide decreases on N doping, which is very similar to our previous observation.²⁸ In the present investigation, the PL intensity of N-GZ mixed oxide is decreased after RGO introduction. Among all, 4 wt % loading of RGO to N-GZ shows the lowest PL intensity, which indicates that more nonexcited electrons are trapped and stably transferred through the interface and lower recombination rate.⁴⁹ Hence, 4RGO/N-GZ shows highest photocatalytic activity compared to all other prepared composites, but the PL intensity of 5RGO/N-GZ is higher than 4RGO/N-GZ, which may be due to a considerable decrease in both the absorption of light and the generation of electrons (e^-)- holes (h^+) pairs on a high amount of RGO loading to N-GZ.^{39,40}

4.8. Time-Resolved Photoluminescence Spectra. Time-resolved photoluminescence measurement of GZ, N-GZ, and 4RGO/N-GZ mixed oxide has been carried out to

calculate decay components which give the brief idea about the photoexcited electron (e^-) transfer dynamics. Figure 7 illustrates the time-resolved photoluminescence spectra for GZ, N-GZ, and 4RGO/N-GZ mixed oxide nanocomposite.

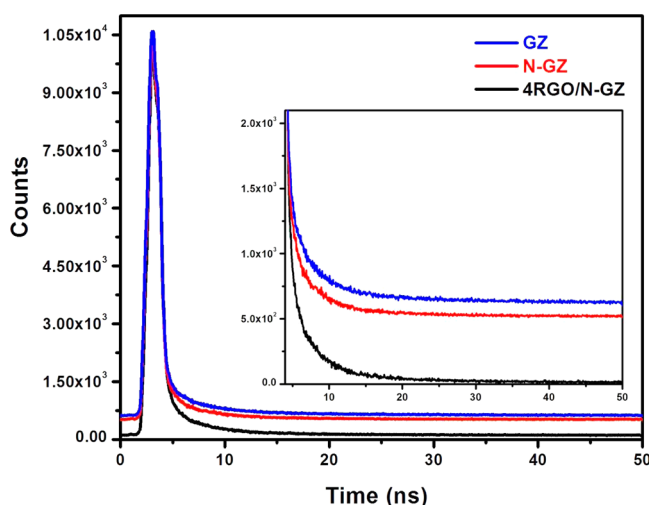


Figure 7. Time-resolved photoluminescence spectra for GZ, N-GZ, and 4RGO/N-GZ mixed oxide nanocomposite.

trates the time-resolved photoluminescence spectra of GZ, N-GZ, and 4RGO/N-GZ mixed oxide. Table 2 represents the well fitted decay dynamics for GZ, N-GZ, and 4RGO/N-GZ mixed oxide. It can be clearly observed that 4RGO/N-GZ mixed showed longer decay time value compared neat N-GZ which can be ascribed to the effective charge transfer across the interface of graphene and N-GZ mixed oxide.⁵⁹ In addition to that, the decrease of fractional contribution (f_1 , f_2 , and f_3) and increase in decay time (τ_1 , τ_2 , and τ_3) also suggests the gradual decrease in density of trapped states in the following order, that is, GZ > N-GZ > 4RGO/N-GZ. The lowest density trapped states of 4RGO/N-GZ mixed oxide may be achieved by the well decoration of N-GZ mixed oxide crystal over 2D graphene sheets.⁴⁰ The longer average decay time ($\langle\tau^2\rangle$) of 4RGI/N-GZ mixed oxide than neat N-GZ mixed oxide indicates that graphene presence facilitates the charge separation which enhances its photocatalytic activity.

4.9. Photoelectrochemical Performance. The photocurrent density was measured to evaluate the photoelectrochemical properties of N-GZ mixed oxide and 4RGO/N-GZ composite. Figure 8a and 6b illustrates the photocurrent of N-GZ and 4RGO/N-GZ in dark and light, respectively. Both of the prepared electrodes did not show any photocurrent under dark condition, whereas both N-GZ and 4RGO/N-GZ generate photocurrent in anodic direction under irradiation of light ($\lambda \geq 400$ nm). It has been also observed that this anodic photocurrent of N-GZ and 4RGO/N-GZ gradually increased in the anodic direction and the photocurrent gradually increases with the applied potential, which indicates a good separation of charge carriers with light illumination and also the n-type

semiconductor characteristics of both the photocatalysts.²⁶ In this case, N-GZ and 4RGO/N-GZ exhibit a photocurrent density of 0.13 and 6.49 mA/cm², respectively (Figure 8b). That means the 4RGO/N-GZ composite shows nearly 50× more photocurrent density than neat N-GZ mixed oxide, which suggests that more numbers of free electrons are transported in the circuit in the case of 4RGO/N-GZ photoelectrode. Here RGO possesses an outstanding ability to sink the photo-generated electron and transport it on its extended Π -conjugated carbon network and, hence, reduces the recombination rate of electron–hole pairs. This obtained result from the photoelectrochemical behavior of 4RGO/N-GZ is in good agreement with PL and TRPL studies.

For an n-type semiconductor, the conduction band edge of photoelectrode was estimated from its flat band potential which was considered to be the photocurrent onset potential.²⁶ The N-GZ photoelectrode showed the photocurrent onset potential at -0.59 eV vs Ag/AgCl at pH 5.9. As the estimated band gap energy of N-GZ is 2.6 eV, its valence band maximum was calculated to be 2.01 eV in accordance with the position of the conduction band edge.²⁶ The current potential study reveals that the conduction band edge of N-GZ is more negative than the reduction potential of H^+ and more positive than the water oxidation potential. Thus, it is confirmed that the prepared N-GZ photocatalyst is suitable for both water reduction and oxidation reaction. Moreover, the photocurrent onset potential 4RGO/N-GZ electrode was observed to be -0.6 eV versus Ag/AgCl at pH 5.9. According to the band gap energy, the valence band maximum is calculated to be 1.95 eV by assuming the conduction band edge to be -0.6 eV. So the alignment of the conduction band edge and valence band edge confirmed that the prepared RGO-based N-GZ mixed oxide nanocomposite photocatalysts are suitable for photocatalytic water splitting reaction.

Under continuous irradiation of light, the stability of N-GZ and 4RGO/N-GZ photoelectrodes at a potential of 0.6 eV versus Ag/AgCl is 60 s, which is shown in Figure 8c. The stability study reveals that the 4RGO/N-GZ photoelectrode is very stable compared to the N-GZ photoelectrode. This is due to the strong interaction between N-GZ and RGO, which enhances the photostability of the electrode.

5. PHOTOCATALYTIC HYDROGEN PRODUCTION USING RGO/N-GZ NANOCOMPOSITES

Photoelectrochemical measurement of all synthesized nanocomposites shows a suitable band gap for photochemical water splitting reaction. Under visible light irradiation ($\lambda \geq 400$ nm), the hydrogen evolution experiment was carried out taking 50 mL of 10 vol % methanol solution and 0.05 g of powder photocatalysts. The reference experiments are carried out by taking pure methanol solution in the absence of either photocatalyst or irradiation. It was observed that no hydrogen gas was detected, which suggests that no hydrogen was produced from methanol solution by photocatalytic reaction.

Table 2. Emission Decay Components of GZ, N-GZ, and 4RGO/N-GZ Mixed Oxide Nanocomposite

sample name	decay time (ns)				fractional contribution			goodness of fit parameter (χ^2)
	τ_1	τ_2	τ_3	$\langle\tau\rangle$	f_1	f_2	f_3	
GZ	0.11	1.17	6.43	2.57	0.264	0.21	0.07	1.192
N-GZ	0.16	1.83	9.23	3.74	0.237	0.191	0.04	1.128
4RGO/N-GZ	0.19	2.82	14.27	5.76	0.214	0.176	0.02	1.017

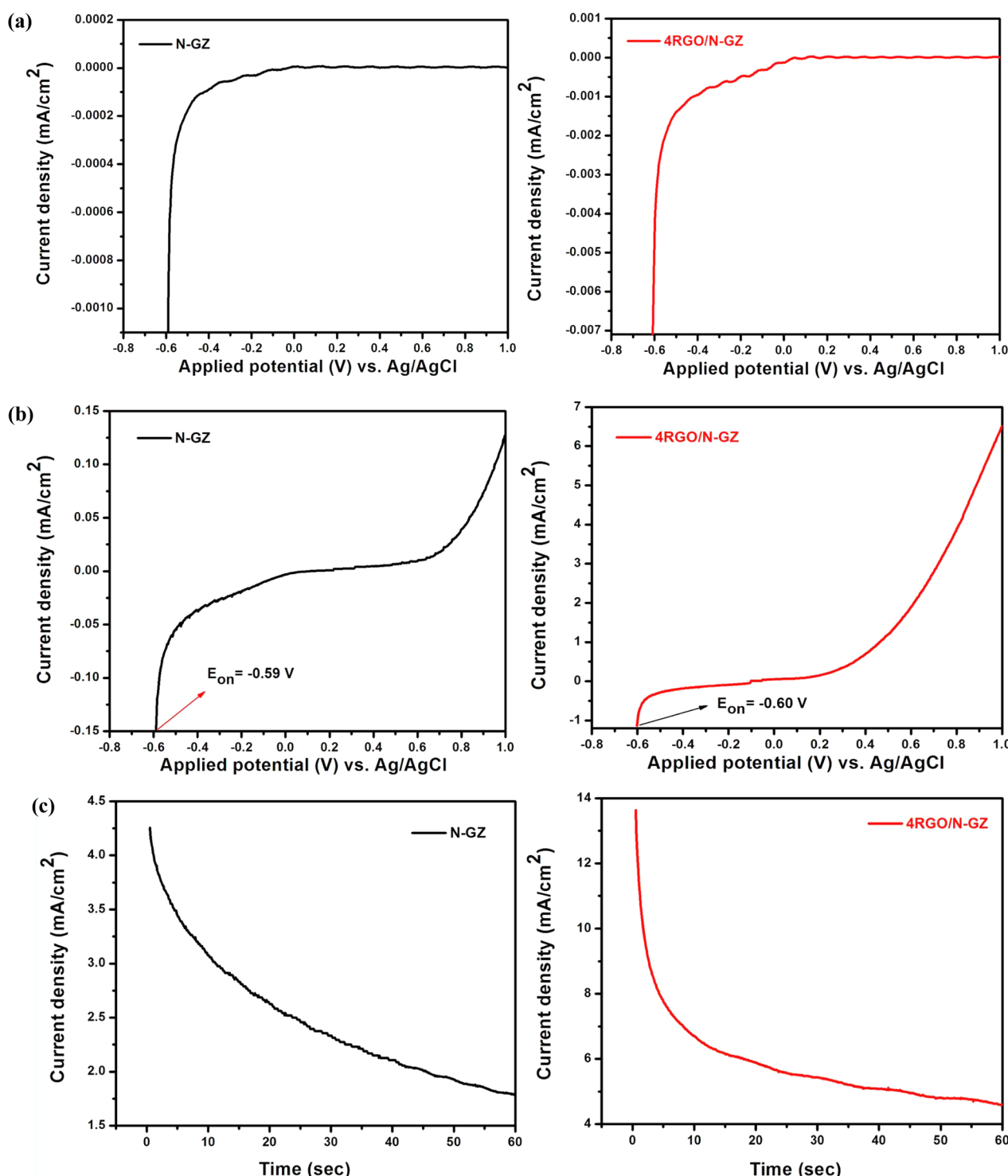


Figure 8. (a) Photocurrent spectra of the N-GZ and 4RGO/N-GZ in dark. (b) Photocurrent spectra of the N-GZ and 4RGO/N-GZ under illumination of visible light ($\lambda \geq 400$ nm). (c) Stability test of N-GZ and 4RGO/N-GZ electrode (current density–time curves) at a potential of 0.6 V vs Ag/AgCl under irradiation of visible light ($\lambda \geq 400$ nm).

Figure 9a represents the amount of H_2 evolution of all the graphene-hybridized N-GZ mixed oxide. From Figure 9a it was observed that all the graphene content photocatalysts showed better hydrogen production activity. The neat N-GZ mixed oxide could able to evolve 523.2 $\mu\text{mol}/\text{h}$ hydrogen gas under visible light irradiation. The hydrogen production activity was significantly increased up to 4 wt % loading amount of graphene. The 1RGO/N-GZ, 3RGO/N-GZ, and 4RGO/N-GZ

nanocomposite photocatalysts could be able to evolve hydrogen gas at 711.4, 830.1, and 894.6 $\mu\text{mol}/\text{h}$, respectively, but this activity decreases at 5 wt % loading amount of graphene. The SRGO/N-GZ could be able to produce 667.2 $\mu\text{mol}/\text{h}$ hydrogen gas under visible light irradiation. This result shows that the higher amount graphene loading (5 wt %) may lead to an increase in the opacity of N-GZ mixed oxide due to its blackbody property and reduces its photocatalytic efficiency.⁵⁸

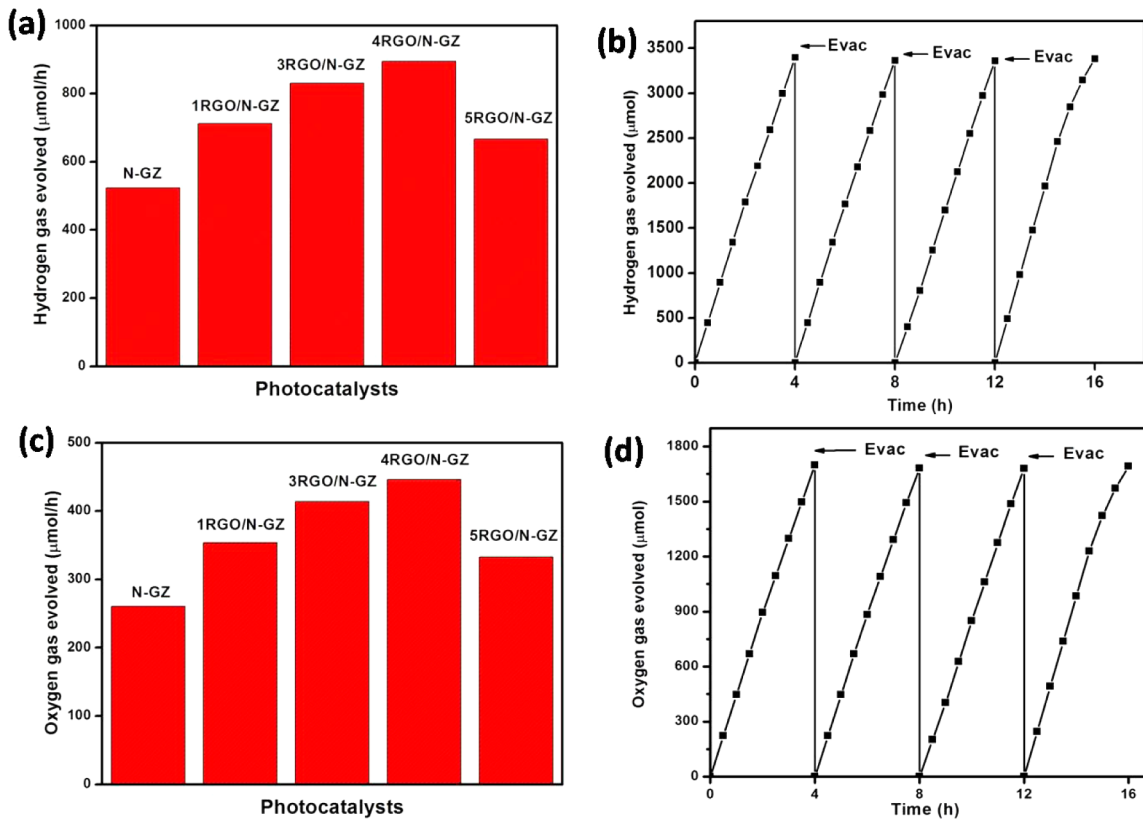


Figure 9. (a) Photocatalytic H_2 evolution over N-GZ, 1RGO/N-GZ, 3RGO/N-GZ, 4RGO/N-GZ, and 5RGO/N-GZ under visible-light irradiation. (b) Time course of H_2 evolution over 4RGO/N-GZ. (c) Photocatalytic O_2 evolution over N-GZ, 1RGO/N-GZ, 3RGO/N-GZ, RGO/N-GZ, and 5RGO/N-GZ under visible-light irradiation. (d) Time course of O_2 evolution over RGO/N-GZ.

In case of graphene-loaded N-GZ mixed oxide, graphene acts as acceptor and transporter. It accepts the photoexcited electrons from the conduction band of N-GZ mixed oxide and channels them through its Π -conjugated network, resulting in the significant inhibition of the recombination of the photoexcited electrons and holes.⁴² So the presence of graphene greatly enhances the hydrogen production activity of N-GZ mixed oxide. However, 5 wt % loading amount of graphene to N-GZ mixed oxide may occupy the active sites on the surface of the photocatalyst, shielding them from incident light to reach the surface of the photocatalysts and consequently resulting in the decrease in the rate of hydrogen evolution.^{39,42} It was also found that neat graphene did not show any photocatalytic activity toward hydrogen production under visible irradiation, which shows its inactivity toward photocatalytic application.

In this investigation, 4RGO/N-GZ showed highest hydrogen gas production under visible light irradiation. Figure 8b illustrates the time course photocatalytic hydrogen production over 4RGO/N-GZ composite. The apparent quantum efficiency was calculated by the following formula:

$$\text{QE} = \frac{2 \times \text{number of } \text{H}_2 \text{ molecules evolved}}{\text{number of incident photons on reacting surface}} \times 100$$

It is observed that the 4RGO/N-GZ composite could evolve a steady rate of hydrogen production, $894.6 \mu\text{mol}/\text{h}$, with an apparent quantum efficiency of 6.3% under visible light irradiation. All the prepared photocatalysts were subjected to perform water oxidation by taking 50 mL of 0.05 M AgNO_3 solution and 0.05 g photocatalysts. Figure 9c,d represents the photocatalytic oxygen evolution results of all the photocatalysts. The neat N-GZ photocatalyst could evolve $260 \mu\text{mol}/\text{h}$

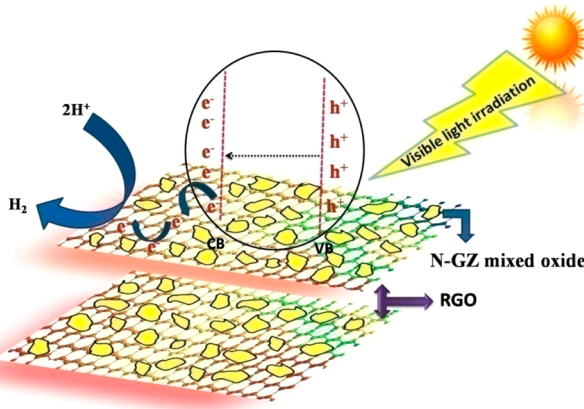
$\mu\text{mol}/\text{h}$ oxygen, whereas all RGO/N-GZ nanocomposite photocatalysts showed high oxygen evolution capacity in comparison to neat N-GZ mixed oxide. The 1RGO/N-GZ, 3RGO/N-GZ, 4RGO/N-GZ, and 5RGO/N-GZ nanocomposites could evolve oxygen gas at 353.8 , 414 , 446.2 , and $332.5 \mu\text{mol}/\text{h}$, respectively. The time course of photocatalytic O_2 production is shown in Figure 9d. The photocatalytic oxygen evolution ability of all RGO/N-GZ nanocomposites maintained the same trend as their photocatalytic hydrogen production results in a stoichiometric ratio of $\sim 2:1$.

5.1. Discussion. The best photocatalytic activity of 4RGO/N-GZ can be explained on the basis of following five important aspects: (1) Presence of RGO; (2) High photocurrent generation; (3) Large BET surface area; (4) Low PL intensity; and (5) Longer average decay time (τ) measured from TRPL analysis.

- (1) RGO played a significant role in enhancing the photocatalytic activity of N-GZ mixed oxide. Generally, the photocatalytic hydrogen production directly depends on the concentration of electrons produced during the photocatalytic reaction. That means, the rate of photocatalytic hydrogen production enhances with the increasing in the concentration of electron. But flash recombination time of electron–hole (10^{-9}s) is a big problem in this field.⁶⁰ It is well-known that graphene acts as an outstanding electron acceptor and possesses electron transporting properties. The X-ray mapping of 4RGO/N-GZ (Figure S2, Supporting Information) shows the uniform distribution of nitrogen in GZ mixed oxide and also the good distribution of each

component over graphene, which confirms the strong interaction between N-GZ and RGO sheets. From TEM analysis (Figure 2), the homogeneous anchored N-GZ nanoparticles on the RGO sheet creates a good transportation of the excited electron to graphene sheets at its interface. Then, this electron can be easily channelized on the II-conjugated carbon network of graphene and effectively inhibits the recombination of charge carriers. The mechanism of photocatalytic hydrogen production is shown in Scheme 2.

Scheme 2. Mechanism of Hydrogen Production over 4RGO/N-GZ Mixed Oxide



- (2) Under visible light irradiation, the enhanced rate of hydrogen production activity of 4RGO/N-GZ is also well proven from its high photocurrent generation. 4RGO/N-GZ showed the photocurrent density of 6.49 mA, which is nearly 50× more than that of N-GZ. From the photocurrent measurement, both N-GZ and 4RGO/N-GZ showed n-type semiconducting character. That means, the concentration of excited electrons is more in 4RGO/N-GZ, which is directly related with its photocatalytic activity. Hence, the 4RGO/N-GZ showed a high rate of hydrogen production under visible light irradiation.
- (3) From BET surface area analysis, 4RGO/N-GZ nanocomposite showed the surface area of $96\text{ m}^2/\text{g}$, which is almost 2× higher than neat N-GZ. This result shows that 4RGO/N-GZ nanocomposite possesses more active sites on its surface for better accommodation of reactant molecule, resulting in better photocatalytic activity.
- (4) PL study of 4RGO/N-GZ also well supports its best photocatalytic activity among all the synthesized photocatalysts. Among all photocatalysts, the lowest PL intensity of 4RGO/N-GZ indicates the minimum recombination process of charge carriers. The minimum rate of recombination of charge carriers gives the evidence for the availability of more free charge carries for photocatalytic reaction. Hence, 4RGO/N-GZ showed highest photocatalytic activity for hydrogen production.
- (5) From the TRPL measurement, 4RGO/N-GZ showed longer decay time than that of neat N-GZ. As TRPL analysis provides the better understanding of e^- transfer dynamics, there is effective charge separation that occurs across the interface of RGO and N-GZ. It may be due to the strong interaction between N-GZ mixed oxide and RGO sheets, which is achieved by the well decoration N-

GZ mixed oxide on RGO sheets. In this addition, the relaxation and decay time also provides the idea about the densities of initial and final states. Hence, the longer decay time ($\langle\tau\rangle$) of 4RGO/N-GZ confirms its better charge separation, which simultaneously enhances its photocatalytic activity for hydrogen production.

6. CONCLUSION

Briefly, a facile two-step chemical route has been adopted for the synthesis of highly active 4RGO/N-GZ mixed oxide composites for photocatalytic hydrogen production. Several characterization techniques, such as XRD, TEM, DRUV-vis, Raman, XPS, BET surface area, PL spectra, TRPL spectra, and photoelectrochemical measurement, were done to characterize the as-prepared composites. The photocatalytic activities of all the composites are well correlated with the results on TEM, PL, TRPL, BET surface area, and photocurrent measurement. The homogeneous anchoring of N-GZ mixed oxide over graphene sheets played a determining role for enhanced photocatalytic activity. Here, graphene acts as cocatalyst, which possesses a lot of potential to accept and transport electrons from the excited N-GZ nanoparticles. This leads to significant lowering of electron–hole recombination and also improves the photocatalytic activity of N-GZ mixed oxide. The loading of graphene to N-GZ mixed oxide strongly affects its photocatalytic activity. However, only 4 wt % loading of graphene to N-GZ mixed oxide showed excellent photocatalytic activity for hydrogen production ($894.6\text{ }\mu\text{mol}/\text{h}$) with an apparent quantum efficiency of 6.3% under visible light irradiation. The correlation of graphene amount with photocatalytic activity is successfully explained. Compared to other synthesized prepared composites, the superior photocatalytic activity of 4RGO/N-GZ is in good agreement with high surface area, high photocurrent density, lowest PL intensity, longer decay time ($\langle\tau\rangle$), and unique property of graphene. Lastly, it can be concluded that the developed composite also has a lot of potential for fuel cell technology and solar cell applications.

■ ASSOCIATED CONTENT

Supporting Information

Additional supporting figures. This material is available free of charge via the Internet at <http://pubs.acs.org>.

■ AUTHOR INFORMATION

Corresponding Author

*E-mail: paridakulamani@yahoo.com, kulamaniparida@soauniversity.ac.in. Tel.: +91-674-2379425. Fax: +91-6 74-2581637.

Notes

The authors declare no competing financial interest.

■ ACKNOWLEDGMENTS

The authors are very much thankful to Prof. B. K. Mishra, Director, CSIR-IMMT for giving permission to publish the work. One of the authors, D. K. Padhi, is thankful to Dr. Y. S. Chaudhary and K. K. Nanda for the TRPL analysis.

■ REFERENCES

- (1) Fujishima, A.; Honda, K. Electrochemical photolysis of water at a semiconductor electrode. *Nature* **1972**, *238*, 37–38.
- (2) Ohno, T.; Bai, Lu.; Hisatomi, T.; Maeda, K.; Domen, K. Photocatalytic water splitting using modified GaN:ZnO solid solution

- under visible light: long-time operation and regeneration of activity. *J. Am. Chem. Soc.* **2012**, *134*, 8254–8259.
- (3) Parida, K. M.; Biswal, N.; Das, D. P.; Martha, S. Visible light response photocatalytic water splitting over CdS-pillared zirconium–titanium phosphate (ZTP). *Int. J. Hydrogen Energy* **2010**, *35*, 5262–5269.
 - (4) Higashi, M.; Domen, K.; Abe, R. Highly stable water splitting on oxynitride TaON photoanode system under visible light irradiation. *J. Am. Chem. Soc.* **2012**, *134*, 6968–6971.
 - (5) Martha, S.; Das, D. P.; Biswal, N.; Parida, K. M. Facile synthesis of visible light responsive $V_2O_5/N/S-TiO_2$ composite photocatalyst: enhanced hydrogen production and phenol degradation. *J. Mater. Chem.* **2012**, *22*, 10695–10703.
 - (6) Kato, H.; Kudo, A. Visible-light-induced H_2 evolution from an aqueous solution containing sulfide and sulfite over a $ZnS-CuInS_2-AgInS_2$ solid-solution photocatalyst. *Angew. Chem., Int. Ed.* **2005**, *44*, 3565–3568.
 - (7) Bang, J. H.; Richard, J. H.; Suslick, K. S. Nanostructured $ZnS:Ni^{2+}$ photocatalysts prepared by ultrasonic spray pyrolysis. *Adv. Mater.* **2008**, *20*, 2599–2603.
 - (8) Leroy, C. L. M.; Maegli, A. E.; Sivula, K.; Hisatomi, T.; Xanthopoulos, N.; Otal, E. H.; Yoon, S.; Weidenkaff, A.; Sanjinesd, R.; Gratzel, M. $LaTiO_2N/In_2O_3$ photoanodes with improved performance for solar water splitting. *Chem. Commun.* **2012**, *48*, 820–822.
 - (9) Lee, S. Photocatalytic water splitting under visible light with particulate semiconductor catalysts. *Catal. Surv. Asia* **2005**, *9*, 217–227.
 - (10) Khan, S. U. M.; Al-Shahry, M.; Ingler, W. B. Efficient photochemical water splitting by chemically modified $n-TiO_2$. *Science* **2002**, *297*, 2243–2245.
 - (11) Sakthivel, S.; Kisch, H. Daylight photocatalysis by carbon-modified titanium dioxide. *Angew. Chem., Int. Ed.* **2003**, *42*, 4908–4911.
 - (12) Luo, H.; Takata, T.; Lee, Y.; Zhao, J.; Domen, K.; Zhao, J.; Yan, Y. Photocatalytic activity enhancing for titanium dioxide by co-doping with bromine and chlorine. *Chem. Mater.* **2004**, *16*, 846–849.
 - (13) Park, J. H.; Kim, S.; Bard, A. J. Novel carbon-doped TiO_2 nanotube arrays with high aspect ratios for efficient solar water splitting. *Nano Lett.* **2006**, *6*, 24–28.
 - (14) Maeda, M. K.; Takata, T.; Hara, M.; Saito, N.; Inoue, Y.; Kobayashi, H.; Domen, K. GaN:ZnO solid solution as a photocatalyst for visible-light-driven overall water splitting. *J. Am. Chem. Soc.* **2005**, *127*, 8286–8287.
 - (15) Sato, J.; Saito, N.; Yamada, Y.; Maeda, K.; Takata, T.; Kondo, J. N.; Hara, M.; Kobayashi, H.; Domen, K.; Inoue, Y. RuO_2 -loaded β - Ge_3N_4 as a non-oxide photocatalyst for overall water splitting. *J. Am. Chem. Soc.* **2005**, *127*, 4150–4151.
 - (16) Hitoki, G.; Ishikawa, A.; Takata, T.; Kondo, J. N.; Hara, M.; Domen, K. Ta_3N_5 as a novel visible light-driven photocatalyst ($\lambda < 600$ nm). *Chem. Lett.* **2002**, *7*, 736–737.
 - (17) Hitoki, G.; Takata, T.; Kondo, J. N.; Hara, M.; Kobayashi, H.; Domen, K. An oxynitride, TaON, as an efficient water oxidation photocatalyst under visible light irradiation ($\lambda \leq 500$ nm). *Chem. Commun.* **2002**, *16*, 1698.
 - (18) Graciani, J.; Alvarez, L. J.; Rodriguez, J. A.; Sanz, J. F. N doping of rutile TiO_2 (110) surface. A theoretical DFT study. *J. Phys. Chem. C* **2008**, *112*, 2624–2631.
 - (19) Batzill, M.; Morales, E. H.; Diebold, U. Influence of nitrogen doping on the defect formation and surface properties of TiO_2 rutile and anatase. *Phys. Rev. Lett.* **2006**, *96*, 026103.
 - (20) Lv, X. J.; Zhou, S. X.; Zhang, C.; Chang, H. X.; Chena, Y.; Fu, W. F. Synergetic effect of Cu and graphene as cocatalyst on TiO_2 for enhanced photocatalytic hydrogen evolution from solar water splitting. *J. Mater. Chem.* **2012**, *22*, 18542–18549.
 - (21) Kim, H. G.; Hwang, D. W.; Kim, J.; Kim, Y. G.; Lee, J. S. Highly donor-doped (110) layered perovskite materials as novel photocatalysts for overall water splitting. *Chem. Commun.* **1999**, 1077–1078.
 - (22) Kato, H.; Asakura, K. Kudo highly efficient water splitting into H_2 and O_2 over lanthanum-doped $NaTaO_3$ photocatalysts with high crystallinity and surface nanostructure. *J. Am. Chem. Soc.* **2003**, *125*, 3082–3089.
 - (23) Sato, J.; Saito, N.; Nishiyama, H.; Inoue, Y. New photocatalyst group for water decomposition of RuO_2 -loaded p-block metal (In, Sn, and Sb) oxides with d^{10} configuration. *J. Phys. Chem. B* **2001**, *105*, 6061–6063.
 - (24) Sato, J.; Kobayashi, H.; Ikarashi, K.; Saito, N.; Nishiyama, H.; Inoue, Y. Photocatalytic activity for water decomposition of RuO_2 -dispersed Zn_2GeO_4 with d^{10} configuration. *J. Phys. Chem. B* **2004**, *108*, 4369–4375.
 - (25) Arai, N.; Saito, N.; Nishiyama, H.; Shimodaira, Y.; Kobayashi, H.; Inoue, Y.; Sato, K. Photocatalytic activity for overall water splitting of RuO_2 -loaded $Y_xIn_{2-x}O_3$ ($x = 0.9$ –1.5). *J. Phys. Chem. C* **2008**, *112*, 5000–5005.
 - (26) Martha, S.; Reddy, K. H.; Biswal, N.; Parida, K. M. Facile synthesis of InGaZn mixed oxide nanorods for enhanced hydrogen production under visible light. *Dalton Trans.* **2012**, *41*, 14107–14116.
 - (27) Martha, S.; Parida, K. M. Fabrication of nano N-doped $In_2Ga_2ZnO_7$ for photocatalytic hydrogen production under visible light. *Int. J. Hydrogen Energy* **2012**, *37*, 17936–17946.
 - (28) Parida, K. M.; Martha, S.; Das, D. P.; Biswal, N. Facile fabrication of hierarchical N-doped GaZn mixed oxides for water-splitting reactions. *J. Mater. Chem.* **2010**, *20*, 7144–7149.
 - (29) Martha, S.; Reddy, K. H.; Parida, K. M.; Satapathy, P. K. Enhanced photocatalytic activity over N-doped GaZn mixed oxide under visible light irradiation. *Int. J. Hydrogen Energy* **2012**, *37*, 115–124.
 - (30) Mukherji, A.; Seger, B.; Lu, G. Q.; Wang, L. Nitrogen doped $Sr_2Ta_2O_7$ coupled with graphene sheets as photocatalysts for increased photocatalytic hydrogen production. *ACS Nano* **2011**, *5*, 3483–3492.
 - (31) Rao, C. N. R.; Sood, A. K.; Subrahmanyam, K. S.; Govindaraj, A. Graphene: The new two-dimensional nanomaterial. *Angew. Chem., Int. Ed.* **2009**, *48*, 7752–7777.
 - (32) Lee, C.; Wei, X.; Kysar, J. W.; Hone, J. Measurement of the elastic properties and intrinsic strength of monolayer graphene. *Science* **2008**, *321*, 385–388.
 - (33) He, J.; Niu, C.; Yang, C.; Wang, J.; Su, X. Reduced graphene oxide anchored with zinc oxide nanoparticles with enhanced photocatalytic activity and gas sensing properties. *RSC Adv.* **2014**, *4*, 60253–60259.
 - (34) Liu, S.; Liu, C.; Wang, W.; Cheng, B.; Yu, J. Unique photocatalytic oxidation reactivity and selectivity of TiO_2 –graphene nanocomposites. *Nanoscale* **2012**, *4*, 3193–3200.
 - (35) Huang, H.; Yue, Z.; Li, G.; Wang, X.; Huang, J.; Dua, Y.; Yang, P. Heterostructured composites consisting of In_2O_3 nanorods and reduced graphene oxide with enhanced interfacial electron transfer and photocatalytic performance. *J. Mater. Chem. A* **2014**, *2*, 20118–20125.
 - (36) Xiang, Q.; Yu, J.; Jaroniec, M. Synergetic effect of MoS_2 and graphene as cocatalysts for enhanced photocatalytic H_2 production activity of TiO_2 nanoparticles. *J. Am. Chem. Soc.* **2012**, *134*, 6575–6578.
 - (37) Dang, H.; Dong, X.; Dong, Y.; Huang, J. Facile and green synthesis of titanate nanotube/graphene nanocomposites for photocatalytic H_2 generation from water. *Int. J. Hydrogen Energy* **2013**, *38*, 9178–9185.
 - (38) Xu, H.; Li, X.; Kang, S.; Qin, L.; Li, G.; Mu, J. Noble metal-free cuprous oxide/reduced graphene oxide for enhanced photocatalytic hydrogen evolution from water reduction. *Int. J. Hydrogen Energy* **2014**, *39*, 11578–11582.
 - (39) Pradhan, G. K.; Padhi, D. K.; Parida, K. M. Fabrication of α - Fe_2O_3 nanorod/RGO composite: a novel hybrid photocatalyst for phenol degradation. *ACS Appl. Mater. Interfaces* **2013**, *5*, 9101–9110.
 - (40) Padhi, D. K.; Parida, K. M. Facile fabrication of α -FeOOH nanorod/RGO composite: a robust photocatalyst for reduction of Cr(VI) under visible light irradiation. *J. Mater. Chem. A* **2014**, *2*, 10300–10312.
 - (41) Padhi, D. K.; Pradhan, G. K.; Parida, K. M.; Singh, S. K. Facile fabrication of $Gd(OH)_3$ nanorod/RGO composite: Synthesis,

characterisation and photocatalytic reduction of Cr(VI). *Chem. Eng. J.* **2014**, *255*, 78–88.

(42) Martha, S.; Padhi, D. K.; Parida, K. M. Reduced graphene oxide/InGaZn mixed oxide nanocomposite photocatalysts for hydrogen production. *ChemSusChem* **2014**, *7*, 585–597.

(43) Hummers, W. S.; Offeman, R. E. Preparation of graphitic oxide. *J. Am. Chem. Soc.* **1958**, *80*, 1339.

(44) Ikarashi, K.; Sato, J.; Kobayashi, H.; Saito, N.; Nishiyama, H.; Inoue, Y. Photocatalysis for water decomposition by RuO₂-dispersed ZnGa₂O₄ with d¹⁰ configuration. *J. Phys. Chem. B* **2002**, *106*, 9048–9053.

(45) Seema, H.; Kemp, K. C.; Chandra, V.; Kim, K. S. Graphene–SnO₂ composites for highly efficient photocatalytic degradation of methylene blue under sunlight. *Nanotechnology* **2012**, *23*, 355705.

(46) Zhang, L. W.; Fu, H. B.; Zhu, Y. F. Efficient TiO₂ photocatalysts from surface hybridization of TiO₂ particles with graphite-like carbon. *Adv. Funct. Mater.* **2008**, *18*, 2180–2189.

(47) Zhang, Y.; Tang, Z. R.; Fu, X.; Xu, Y. J. TiO₂–graphene nanocomposites for gas-phase photocatalytic degradation of volatile aromatic pollutant: Is TiO₂–graphene truly different from other TiO₂–carbon composite materials? *ACS Nano* **2010**, *4*, 7303–7314.

(48) Valentin, C. D.; Pacchioni, G.; Selloni, A.; Livraghi, S.; Giannello, E. Characterization of paramagnetic species in N-doped TiO₂ powders by EPR spectroscopy and DFT calculations. *J. Phys. Chem. B* **2005**, *109*, 11414–11419.

(49) Shah, M. S. A. S.; Zhang, K.; Park, A. R.; Kim, K. S.; Park, N. G.; Parkab, J. H.; Yoo, P. J. Single-step solvothermal synthesis of mesoporous Ag–TiO₂-reduced graphene oxide ternary composites with enhanced photocatalytic activity. *Nanoscale* **2013**, *5*, 5093–5101.

(50) Shah, M. S. A. S.; Park, A. R.; Zhang, K.; Park, J. H.; Yoo, P. J. Layer-by-layer assembly of polyelectrolyte multilayers in three-dimensional inverse opal structured templates. *ACS Appl. Mater. Interfaces* **2012**, *4*, 2107–2115.

(51) Behera, G. C.; Parida, K. M.; Satapathy, P. K. Sustainable and efficient protocol for the synthesis of a RGO–VPO composite with synergistic stability and reactivity. *RSC Adv.* **2013**, *3*, 4863–4866.

(52) Shah, M. S. A. S.; Park, A. R.; Zhang, K.; Park, J. H.; Yoo, P. J. Green synthesis of biphasic TiO₂-reduced graphene oxide nanocomposites with highly enhanced photocatalytic activity. *ACS Appl. Mater. Interfaces* **2012**, *4*, 3893–3901.

(53) Mkhoyan, K. A.; Contryman, A. W.; Silcox, J.; Stewart, D. A.; Eda, G.; Mattevi, C.; Miller, S.; Chhowalla, M. Atomic and electronic structure of graphene-oxide. *Nano Lett.* **2009**, *9*, 1058–1063.

(54) Tuinstra, F.; Koenig, J. L. Raman spectrum of graphite. *J. Chem. Phys.* **1970**, *53*, 1126.

(55) Kim, J. S.; Kang, H. I.; Kim, W. N.; Kim, J. I.; Choi, J. C.; Park, H. L.; Kim, G. C.; Kim, T. W.; Hwang, Y. H.; Mho, S. I.; Jung, M. C.; Han, M. Color variation of ZnGa₂O₄ phosphor by reduction-oxidation processes. *Appl. Phys. Lett.* **2003**, *82*, 2029.

(56) Boppana, V. B. R.; Doren, D. J.; Lobo, R. F. Analysis of Ga coordination environment in novel spinel zinc gallium oxy-nitride photocatalysts. *J. Mater. Chem.* **2010**, *20*, 9787–9797.

(57) Mahmood, K.; Park, S. B.; Sung, H. J. Enhanced photoluminescence, raman spectra and field-emission behavior of indium-doped ZnO nanostructures. *J. Mater. Chem. C* **2013**, *1*, 3138–3149.

(58) Qiu, J.; Zhang, P.; Ling, M.; Li, S.; Liu, P.; Zhao, H.; Zhang, S. Photocatalytic synthesis of TiO₂ and reduced graphene oxide nanocomposite for lithium ion battery. *ACS Appl. Mater. Interfaces* **2012**, *4*, 3636–3642.

(59) Nanda, K. K.; Swain, S.; Satpati, B.; Besra, L.; Chaudhary, Y. S. Facile synthesis and the photo-catalytic behavior of core–shell nanorods. *RSC Adv.* **2014**, *4*, 10928–10934.

(60) Tian, J.; Liu, S.; Zhang, Y.; Li, H.; Wang, L.; Luo, Y.; Asiri, A. M.; Al-Youbi, A. O.; Sun, X. Environmentally friendly, one-pot synthesis of Ag nanoparticle-decorated reduced graphene oxide composites and their application to photocurrent generation. *Inorg. Chem.* **2012**, *51*, 4742–4746.